Applied Surface Science 597 (2022) 153685

Contents lists available at ScienceDirect

Applied Surface Science

journal homepage: www.elsevier.com/locate/apsusc

Full Length Article

# Tunable fluorescence and magnetic properties of ceria- organic core- shell hollow structures

Hao-Cheng Chien [a], Bo-You Wu [a], Pei-Kai Hsu [a], Yi-Che Chen [a], Jenn-Ming Song [b], Alexandre Gloter [c,*], Shih-Yun Chen [a,*]

[a] Department of Materials Science and Engineering, National Taiwan University of Science and Technology, Taipei, Taiwan
[b] Department of Materials Science and Engineering, National Chung Hsing University, Taichung 402, Taiwan
[c] Laboratoire de Physique des Solides, Université Paris-Saclay, CNRS UMR 8502, F-91405 Orsay, France

A B S T R A C T

In this study, mesoscopic ceria- organic core–shell hollow spheres with tunable luminescence and magnetism were demonstrated. The organic layer was grown on the surface of ceria hollow spheres by the reaction of citric acid solution and ethylenediamine via hydrothermal process. With increasing the reaction time from 0 to 6 h, the organic phase varies from discontinuous carbon- rich dots to a nanometrical layer which contains randomly distributed $Ce^{3+}$- rich clusters. The growth process of the surface organic phase accelerates the formation of defect layers on the surface of ceria hollow spheres, while inhibiting further reduction inside the ceria shell. The synergistic effect formed by the structural changes of the surface organic phase and underlying ceria enables all samples to exhibit ferromagnetic and luminescent properties at room temperature. The ferromagnetic strength closely depends on the continuity and defect content of the $Ce^{3+}$-rich layer on the surface of the ceria hollow spheres. The enhanced fluorescence, especially the blue and red emissions, is attributed to the defective structure of ceria and the composition of the organic phase.

## 1. Introduction

The crystal structure of ceria is cubic fluorite structure with $Ce^{4+}$ at the FCC sites and $O^{2-}$ ions at the tetrahedral sites. One of the characteristics of $CeO_2$ is that it can maintain its crystal structure even with a large numbers and types of defects, giving a playground for defect engineering. Via the defect chemistry and the nano-size effects, many technological advances have been obtained in $CeO_2$-based nanomaterials, notably for environmental applications [1,2]. Since the defects associated with the formation of oxygen vacancies, including $Ce^{3+}$ or $F^0$ centers, were found to be efficient luminescent centers, optical engineering of ceria by manipulating various types of defects has also begun to attract discussions [3,4,5,6,7].

In the past two decades, due to the rise of spintronics and magnetic oxides, a considerable number of researchers have been involved in the study of defect engineering in ceria nanostructures for the regulation of magnetic properties. Three main approaches have been followed on that aspect : (1) *Doping*; various elements, including magnetic transition metals and nonmagnetic rare earth elements have been doped into ceria [8,9,10,11]. (2) *Reduction*; it has been found that the oxygen vacancies can be introduced into $CeO_2$ through post reduction process. Magnetic behavior of $CeO_2$ was found to be closely related on the character of oxygen vacancies, in particular the one at surface [12,13,14]. (3) *Surface/ interface effect*; it has been demonstrated that the formation of interface between $CeO_2$ and other phase causes the aggregation of $Ce^{3+}$ within a thin layer at interface. The magnetic properties of samples with such interfacial defect distribution were significantly improved [15,16].

From the above-mentioned relationships between defect engineering and magnetic properties, the structural characteristics of hollow spheres seem to be favorable for the enhancement of magnetic strength. There have been some reports investigating the magnetic properties of oxide hollow spheres [17,18]. Different processes have been utilized to control the surface structure and defects, including the reaction with acid or annealing, which can indeed increase the magnetic strength of the sample [19]. However, while increasing the amount of defects on the surface of the sphere, how to stabilize its state is a problem that needs to be considered.

Coating an amorphous carbon film is expected to protect the underlying oxide layer from environmental degradation [20]. In composites such as $V_2O_3$/amorphous carbon film [21], $CeO_2$/C [22], and ZnO/C [23], the photocatalytic properties, electrochemical properties, and electrical conductivity were significantly improved. Magnetic changes due to charge transfer at the interface have also been observed in magnetic nanoparticle/amorphous carbon composites [24,25].

In this study, we developed a hollow core–shell structure. Its core is a micron-sized $CeO_2$ hollow sphere prepared by spray pyrolysis method,

* Corresponding authors.

https://doi.org/10.1016/j.apsusc.2022.153685
Received 8 March 2022; Received in revised form 5 May 2022; Accepted 12 May 2022
Available online 23 May 2022

and then an organic carbon layer is deposited on its surface. The organic surface layer was growth by the reaction of citric acid solution and ethylenediamine via hydrothermal process, which has been used to synthesize luminescent quantum carbon dots (CQDs) [26]. The controlled synthesis and the accurate structure determination of CQDs is also of broad interest, notably with the aim of obtaining thin film for integrating them in solid state [27]. Several works reported function-alization of oxide photo-catalytic material by CQDs, for instance, $TiO_2$ with graphene quantum dots [28], $Nb_2O_6$ with $C_3N_4$ QDs [29] or CQDs on cuprous oxide [30]. However, report related to hybrid CQDs and $CeO_2$ is quite rare [31].

Characterization of hybrid organic inorganic system at the nanoscale is rather difficult. CQDs as well as its composites are often determined by bulk measurement such as XPS [31]. Here we show another possibility by using STEM-EELS. With the measurement of C-*K* and Ce-*M* at the nano-scale, the evolution of the continuity and size of CQDs as well as the changes of the ceria oxide when carbonization is done directly on the metal oxide surface can be both unraveled. At last, the defect derived magnetism as well as the luminescence could be discussed with respect to these structural insights.

## 2. Experimental procedure

Ceria- organic core- shell composites were obtained by a two-step process, as illustrated in Fig. S1. At first, $CeO_2$ hollow spheres were prepared using a spray pyrolysis (SP) method. Detailed synthesis process has been described in elsewhere [18]. Next, carbon layer was deposited on the surface of the obtained ceria hollow spheres by reacting with citric acid and ethylenediamine via hydrothermal process. First, 0.025 g of cerium oxide hollow spheres were added to 20 ml of deionized water, followed by 1.05 g of citric acid and 335 μL of ethylenediamine. The mixed solution was then transferred to an autoclave lined with poly-tetrafluoroethylene (Teflon) and heated at 200 °C for 3 to 6 h. The ob-tained composites were then cleaned using centrifugation several times and then dried at 80 °C.

The crystal structure of all samples were determined by using X-ray powder diffractometer (XRD) with Cu $K_\alpha$ radiation (Bruker D2 PHASER XE-T XRD) and Raman scattering spectrometer (HORIBA iHR550) with an excitation wavelength of 532 nm. The microstructure were investi-gated using transmission electron microscopy (TEM) with accelerate voltage to be 200 keV (FEI Tecnai™ G2 F-20 S-TWIN, FEI Talos F200XG2). Scanning transmission electron microscopy (STEM), high angle annular dark field (HAADF) and electron energy loss spectroscopy (EELS) analysis were performed using a Cs corrected STEM NION operating at 100 keV. The X-ray absorption analysis was performed the National Synchrotron Radiation Research Center (NSRRC), Taiwan. O *K*-edge and Ce $M_{4,5}$ edge were recorded at HSGM beamline 20A with the energy resolution was about 0.017 eV and 0.01 eV respectively. Ce $L_3$-edge was recorded at a DCM tender X-ray beamline 16A with energy resolution to be 0.25 eV. The magnetic properties were measured using a vibrating sample magnetometer (VSM) at room temperature at the Institute of Physics, Academia Sinica, Taiwan. The photoluminescence spectra was obtained by Jasco FP-6300 spectrofluorometer. Fluorescent images were recorded on a Leica TCS SP5 Laser Scanning Confocal Mi-croscope. Excitation of the samples was performed by a laser of $\lambda = 488$ and 561 nm, and emission was recorded in the range from 500 nm to 600 nm and 601 to 701 nm, respectively.

## 3. Results and discussion

### 3.1. Microstructures of organic- $CeO_2$ core shell hollow spheres

First, the phase determination and the morphology investigation of the as-prepared ceria spheres was studied. XRD pattern of the ceria sphere before reaction shows that there is no other crystalline phase (Fig. S2 (a)). The morphology of the ceria spheres has been investigated by SEM (Fig. S2 (b)). The $CeO_2$ sphere size distribution is plotted in Fig. S2 (c), showing that the $CeO_2$ sphere diameter ranges from 100 nm to 2 μm. Fig. S2 (d) shows the cross sectional TEM image, confirming that the spheres are hollow and the shell thickness is about 30 nm. XRD pattern of $CeO_2$ hollow spheres after reacting with citric acid solution and ethylenediamine for different times (3 to 6 h) is shown in Fig. 1 (a). No other crystalline phases were found, and all the peaks corresponded to the FCC structure of $CeO_2$ standard sample (JCPDS 34–0394). The strong diffraction peaks indicate the high crystallinity of all samples.

Then Raman analysis was performed to identify the vibration state in the sample. Raman spectrum of the vibration state between Ce and O is shown in Fig. 1 (b). The characteristic $F_{2g}$ band and a weak *D* band were detected in all samples. For the $F_{2g}$ band, as the reaction time increases, a band shift and broadening were observed, predicting the weakening of the bonding between Ce and O as well as the formation of defects in the sample [32]. In the insert figure, it is seen that as the reaction time reaches 4.5 h, the change rate of the $F_{2g}$ band slows down. The enlarged *D* bands were shown in Fig. 1 (c), and the relation between the intensity of the *D* band and reacting time is plotted in the insert. It shows that the amount of oxygen vacancy related defects reached maximum in the 3-hour sample and then decreased.

In Fig. 1 (d), two distinct characteristic bands related to carbon can be observed in all samples. The first band located at 1540–1600 $cm^{-1}$ is *G* band, which is assigned to the $E_{2g}$ phonon of $sp^2$ states. The second band located around 1350 $cm^{-1}$ is *D* band. It is attributed to the $A_{1g}$ symmetry and indicates the disorder in the graphite lattice that is caused by the defects in the form of vacancies and grain boundaries [33]. In an ideal graphite structure, all carbon atoms are bonded in the form of $sp^2$, so only *G* band can be detected. When there are defects in the carbon structure or $sp^3$ carbon bonding, the carbon structure tends to be disordered, which leads the *D* band to become obvious [34,35]. In this figure, it is observed that *G* band does not change with increasing the reaction time, while *D* band grows gradually. The upward trend is particularly obvious when the reaction time is longer than 4.5 h. The extent of disorder and the ratio of $sp^3$ /$sp^2$ of carbons was presented by the intensity ratio $I_D/I_G$ and was plotted in the insert. It is seen that the $I_D/I_G$ ratio is inversely proportional to the reaction time, indicating that the surrounding structure of carbon atoms in the sample tends to be disordered, and the proportion of $sp^3$ forms in the carbon bonds grad-ually increases [36,37,38].

The electronic structure of all samples was determined by XAS. The O-*K* edge XANES is shown in Fig. 2 (a). Three distinct absorption edges, *A, B,* and *C* can be observed in all samples. Peak *A* reflects the hybrid-ization of O 2*p*-Ce $4f^0$. Peak *B* and *C* are caused by the splitting of the crystal field in the 5*d* orbital of Ce. A decrease in the intensity of peak *A* and a shift of peak *B* was observed as the reaction time increases, implying that the hybridization between Ce and O decreases after the reaction. The change is particular obvious as the reaction time reaches 4 h.

Ce $M_5$ edge X-ray absorption near edge structure (XANES) of all samples is shown in Fig. 2 (b), three characteristic edges are observed. Peak *D'* presents the contribution form $Ce^{3+}$. With the reaction time increases, it is seen that both peak *D* and *Y* decrease while peak *D'* rises. The enhancement of peak *D'* is obvious in particular in sample after reacting for longer than 4.5 h.

The charge state of Ce of the sample can be estimated based on Ce *L* edge. The Ce *L* edge XANES is shown in Fig. 2 (c). Ce-$L_3$ edge is contributed by the transitions from Ce $2p_{3/2}$ to the 5*d* empty states. All the spectra were first subtracted by an arctangent function to eliminate the background of the electron transition to continuum state and then fitted by five Gaussian functions [39]. Among these, peak *A* is the final energy state $\underline{2p}4f^0 5d^*$ of $Ce^{4+}$, and $\underline{2p}$ means that there is a hole in the 2*p* (J = 3/2) orbital. 5*d** means that there is an excited electron in the 5*d* orbital. The splitting of peak A into $A_1$ and $A_2$ is attributed to the crystal field splitting. Peak *B* is the final energy state $\underline{2p}4f^1 5d^*\underline{L}$ of $Ce^{4+}$, and $\underline{L}$ means a hole generated in the oxygen *p* orbital. Peak *C* corresponds to a

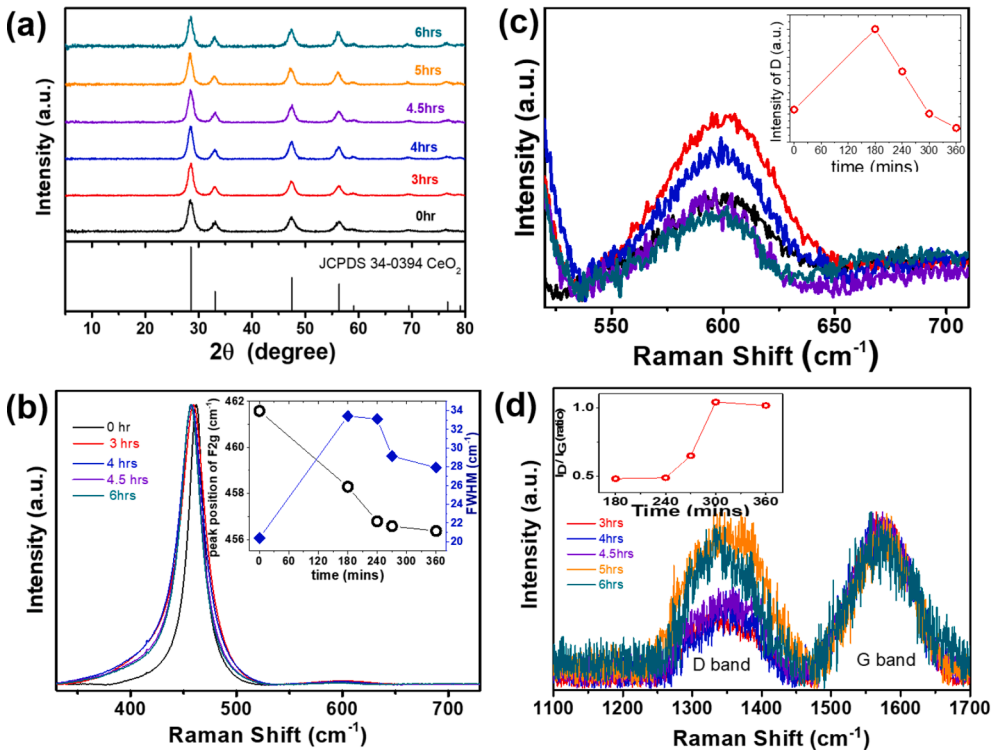


**Fig. 1.** (a) XRD pattern of $CeO_2$ hollow spheres after reacting with citric acid solution for different times (0 to 6 h). (b) Raman spectrum of the vibration state between Ce and O. (c) The enlarged *D* bands. (d) Two characteristic Raman bands related to carbon.

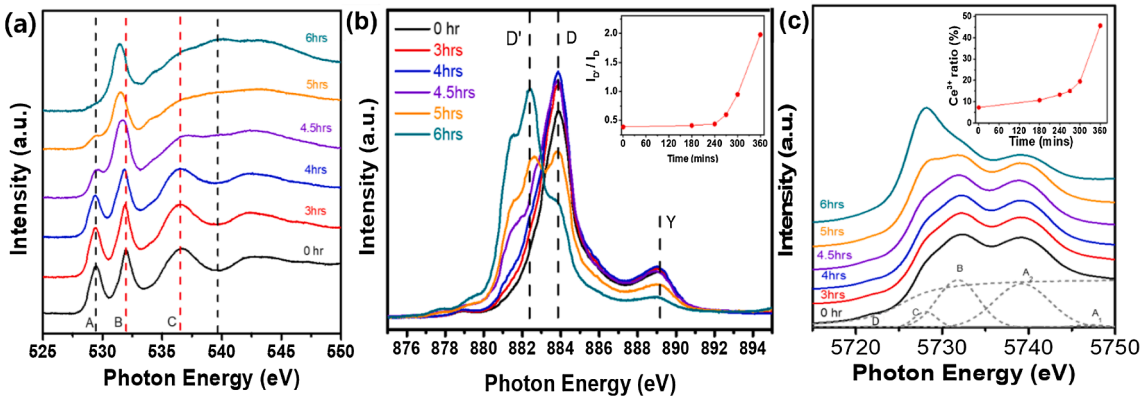


**Fig. 2.** (a) O-*K* edge XANES, (b) Ce $M_5$ edge XANES, and (c) Ce *L* edge XANES of the citric acid treated samples.

transition from the initial electron configuration $\underline{2p}4f^15d^0$ to the $\underline{2p}4f^15d^*$ final state. Peak *D* is attributed to the dipole-forbidden transition from $2p_{3/2} \rightarrow 4f$. The detailed spectral fitting results are shown in Fig. S4. Among the aforementioned components, component C represents the trivalent Ce. Therefore, the concentration of $Ce^{3+}$ in the $CeO_2$ matrix can be expressed as the ratio $I_C/I_{total}$, where $I_C$ is the intensity of the C peak and $I_{total}$ is the sum of the five deconvoluted peaks. The estimated $Ce^{3+}$ content is 7%, 10%, 13%, 15%, 20%, and 46% of sample after reacting for 0-hour, 3-hour, 4-hour, 4.5-hour, 5-hour and 6-hour, respectively. The increasing trend of the $Ce^{3+}$ content observed by Ce *L* edge is consistent with that in Ce *M* edge.

Based on the above spectrum analysis, it can be inferred that when the reaction time exceeds 4 h, the microstructure of the sample will change greatly. In order to show the structural difference caused by the reaction time, TEM cross-sectional analysis was performed on the 4-hour sample and 6-hour sample. Several interesting phenomenon was observed. First, it was found that all samples maintained the hollow sphere structure after the reaction, even if the reaction time is as long as 6 h (Fig. 3 (a) and (b)). Second, no other phase is observed on the surface of the 4 h-sample (Fig. 3 (c)) while an amorphous layer is seen on both the outer and the inner surface in the 6-hour sample (Fig. 3 (d)). The amorphous layer can be observed on the surface of hollow spheres of different sizes, as shown in Fig. S4. The thickness of the amorphous layer is about 10 to 20 nm. At last, high resolution TEM (HRTEM) observations revealed clear lattice fringes in the ceria shell of both the 4-hour and the 6-hour samples (Fig. 3 (e) and (f)). The high crystallinity observed by TEM in the 6-hour sample contradicts the XAS analysis, which shows that the $Ce^{3+}$ content is as high as 46%.

STEM/EELS was utilized to investigate the spatial distribution of elements and valence. Spheres after reacting for 4.5 h were investigated first. Fig. 4 (a) is the STEM/HAADF image obtained from the surface of the 4.5-hour sample. Fig. 4 (b) is the EELS C-*K* maps and the spectra obtained from the thin surface layer and particle like structure. The layer is consist of C, Ce, and O, with a thickness of ca. 1–2 nm. Furthermore,

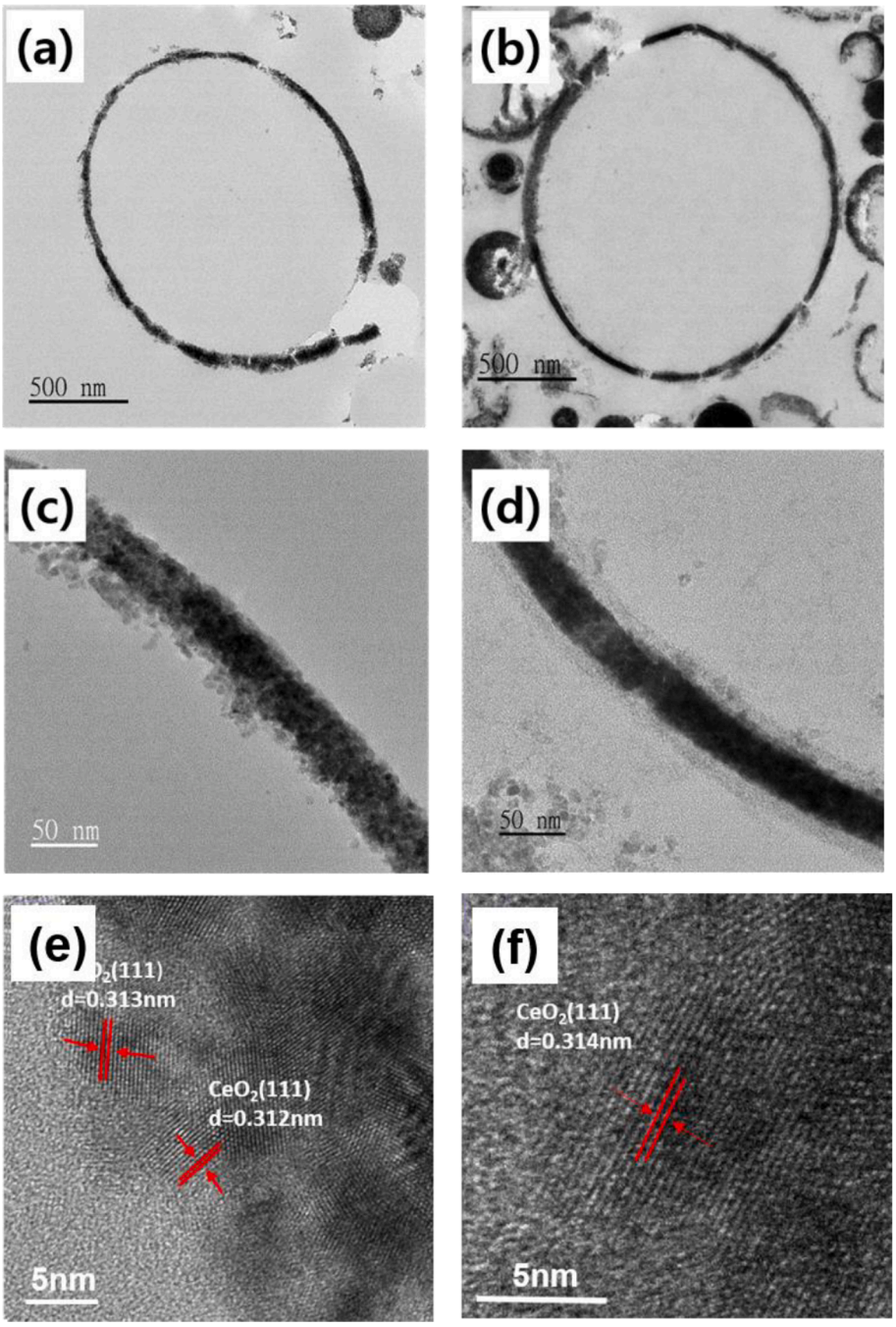


**Fig. 3.** TEM cross-sectional investigations of the 4-hour and 6-hour sample. (a) (c) and (e) are cross section of a hollow sphere, part of the shell, and high resolution image of sphere surface of 4-hour sample. (b) (d) and (f) are cross section of a hollow sphere, part of the shell, and high resolution image of sphere surface of 6-hour sample.

some thicker carbon-rich parts where high content of nitrogen and a small amount of cerium are also observed (blue box). An enlarged STEM/bright field image (BF) of the ceria shell surface is shown in Fig. 4 (c). Clear fringes were seen, which is consistent with the HRTEM observations. The dark field (DF) image is shown in Fig. 4 (d). Element mapping of C is demonstrated in Fig. 4 (e). A thin but discontinuous carbon-rich layer is present at the surface. Inside the ceria shell, a weak carbon signal was detected. As for the distribution of $Ce^{3+}$, the content is much higher at ceria shell surface than the interior region, as seen in Fig. 4 (f). Above observations indicate the aggregation of $Ce^{3+}$ in ceria sphere surface, however, its intensity is modulated by the presence of carbon layer (with a lower amount of defect below the carbon layer).

STEM/EELS analysis of 6-hour sample is shown in Fig. 5. A clear amorphous second phase was observed on the sphere surface, as shown in the STEM-BF (Fig. 5 (a)) and DF (Fig. 5 (b)). The thickness of the second phase layer reaches ca. 10 nm. EELS C *K*-edge, N *K*-edge, and Ce *M*−edge mapping is demonstrated in Fig. 5 (c), (d) and (e), respectively, showing that the dominant component of the second phase layer is C and N with the Ce in trivalent state (Fig. 5(f)). The microstructure of the carbon rich layer is further investigated by high resolution STEM/HAADF and EELS. As seen in Fig. 5 (g), cluster like structure with size less than 1 nm is observed in the HAADF image. According to the mapping of C *K*-edge (Fig. 5 (h)) and Ce *M*−edge (Fig. 5 (i)), it is found that the composition distribution is inhomogeneous. $Ce^{3+}$-rich clusters appear randomly inside the organic layer. EELS spectrum obtained from Ce-rich and Ce-deficient region is shown in Fig. 5 (j) together,

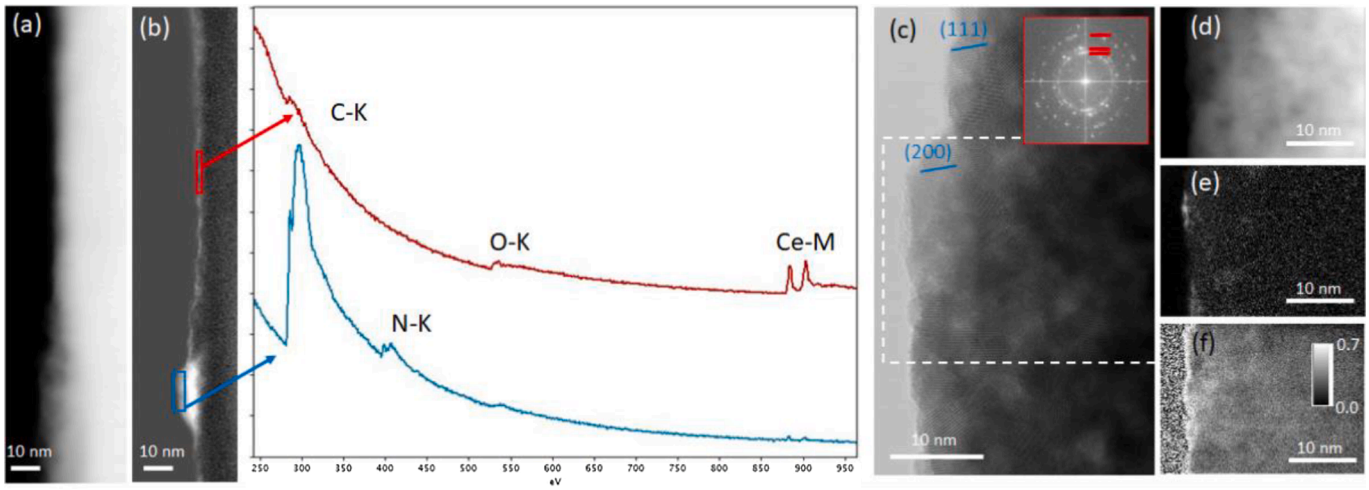


**Fig. 4.** (a) STEM-HAADF and (b) C-K map and spectra obtained at the surface of the sphere. A heterogeneous layer of carbon is observed, with a thickness of ca. 1–2 nm (spectrum from the red box). Furthermore, it can be observed some thicker carbon part where nitrogen and a small amount of cerium are present (spectrum from the blue box). (c) STEM-BF revealing the surface crystallinity of the ceria sphere. A diffraction pattern is in inset with the red bars indicating (1 1 1), (2 0 0) and (1 1 0) ceria planes (d) STEM-HAADF, (e) EELS C-K map and (f) $Ce^{3+}/\Sigma Ce$ map corresponding to the areas boxed in (c). A thin layer of higher $Ce^{3+}$ is present at the surface but its intensity is modulated by the presence of carbon layer. The intensity scale of the $Ce^{3+}/\Sigma Ce$ spans from 0 (black) to 0.7 (white).

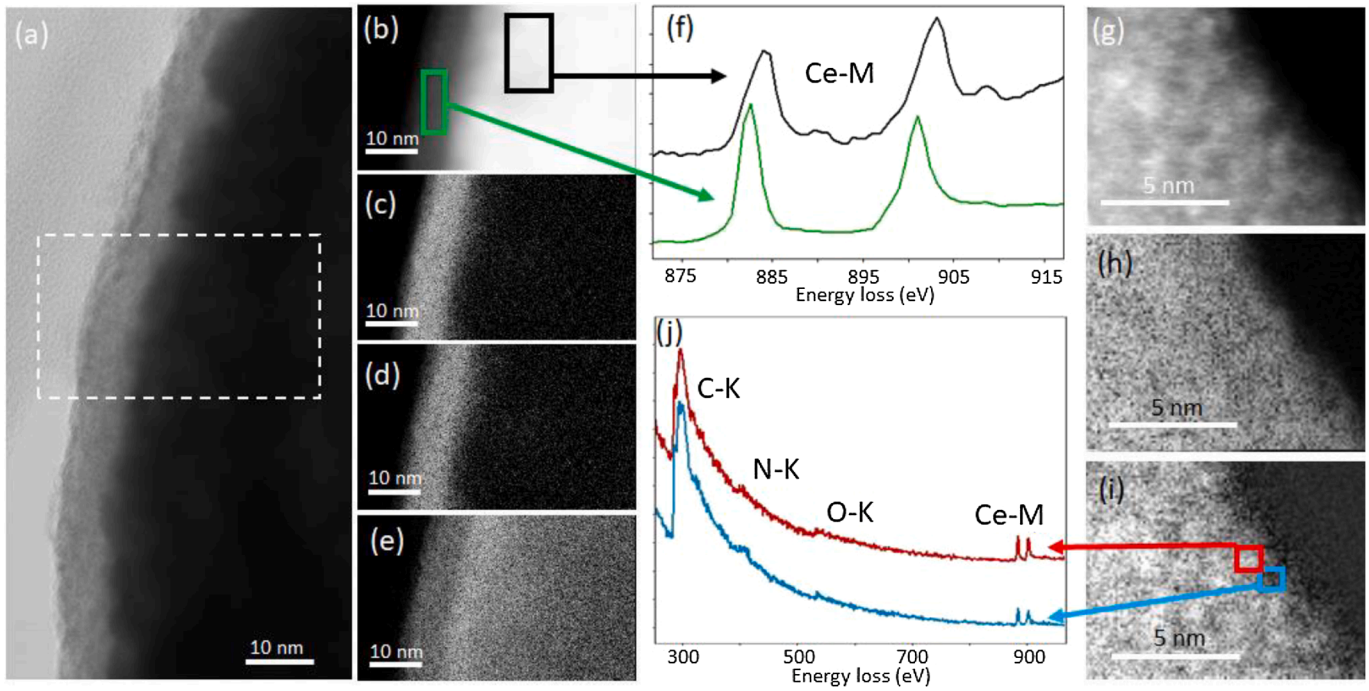


**Fig. 5.** (a) STEM-BF images, (b) STEM-HAADF, (c) EELS C-K, (d) EELS N-K and (e) EELS Ce-M edges maps. A ca. 10 nm thick layer of a Ce-organic complex is continuously present at the surface of the sphere. (f) The EELS Ce-M edge measured for the Ce-organic complex (black spectrum) is for a $Ce^{3+}$ redox state as compared to the $Ce^{4+}$ from the ceria (green spectrum). (g) STEM-HAADF images of the surrounding layer and the corresponding (h) EELS C-K and (i) EELS Ce-M maps. (j) EELS spectra obtained from a Ce-rich and Ce-poor regions as indicated by the red and blue boxes in (i).

confirming the difference in the Ce content.

Consequently, two main characters of the $CeO_2$ hollow sphere microstructure with the deposition of an organic phase on the surface can be concluded. The first is the formation of the thin $Ce^{3+}$-rich ceria layer at ceria sphere surface. Similar phenomenon has been found in $CeO_2$ spheres reacted by nitric acid, in which the $Ce^{3+}$-rich ceria layer is with a thickness ranges from 1 to 5 nm. In present study, it is demonstrated that the aggregation of $Ce^{3+}$ at surface was speeded by the reaction with citric acid and ethylenediamine at high temperature. The obtained $Ce^{3+}$-rich ceria layer is also thinner and more continuous than that of nitric acid treated samples. The second is the structure of the organic layer. It is noted that in this study, as adding $CeO_2$ spheres in precursor, instead of solely nanometer CDs, [26] polymer like carbon-rich layer with nanometer $Ce^{3+}$ rich clusters was obtained. The formation of carbon-rich layer on the sphere surface would inhibit the reduction reaction of underlying ceria sphere. The stabilization of defects near crystal surfaces by surface decoration of organic molecules have also been demonstrated in other oxides [40,41].

### 3.2. Magnetic properties

Fig. 6 (a) is the M−H curves of $CeO_2$ hollow spheres after reacting with citric acid and ethylenediamine for different times. Firstly, it is observed that the magnetic background changed from diamagnetic to paramagnetic as the reaction time reaches 4 h. The strength of paramagnetic background grows as further increasing the reaction time from 4 to 6 h. After the background subtraction, all samples are found to be ferromagnetic at room temperature (Fig. 6 (b)). The highest Ms value was obtained for the 4.5 h sample with a value of 0.005 emu/g, which is comparable to ceria hollow spheres treated by nitric acid and underwent annealing process [15]. In samples with a reaction time of less than 4.5 h, the value of Ms increased with the increase of the reaction time. When the reaction time was higher than 4.5 h, the value of Ms decreased with further increase of the reaction time.

The aforementioned changes in magnetic properties, including the paramagnetic background signal and ferromagnetic strength, are not simply proportional to the reaction time, which can be explained by the synergistic effect of changes in the sample microstructure. The inset of Fig. 6 (c) is a schematic diagram of the structure of the hollow spherical shell surface as a function of reaction time, including the morphology and defect distribution, which are obtained by combining the previous spectroscopic and microscopic analysis results. It shows that when the hollow spheres start to react with citric acid, it will promote the aggregation of $Ce^{3+}$ on the surface, forming a thin defect rich layer. As the reaction time increases, the organic phase begins to appear on the surface of the spheres; when the reaction time increases to more than 4 h, the organic phase extends to cover the entire surface of the spheres, and its thickness gradually increases. The formation of the organic layer was found to prevent the reduction of the underlying ceria. Notably, a large number of nanoscale $Ce^{3+}$-rich clusters appeared in the organic phase. The formation of these $Ce^{3+}$-rich clusters is responsible for the rapid rise in the overall $Ce^{3+}$ content in these long-reacted samples, as shown by the black line in Fig. 6 (c). Considering the paramagnetic properties, it is found that in these organic-ceria hybrid hollow spheres, the enhancement of the paramagnetic background signal is associated with the abnormal increase of $Ce^{3+}$ content. Paramagnetic background was detected in samples that had been reacted for more than 4 h and its strength increased with reaction time. This trend is consistent with the change in the number of $Ce^{3+}$-rich clusters. Therefore, it can be speculated that the paramagnetic background of the organic-ceria hybrid hollow spheres mainly comes from randomly distributed $Ce^{3+}$-rich clusters in the Ce-organic phase.

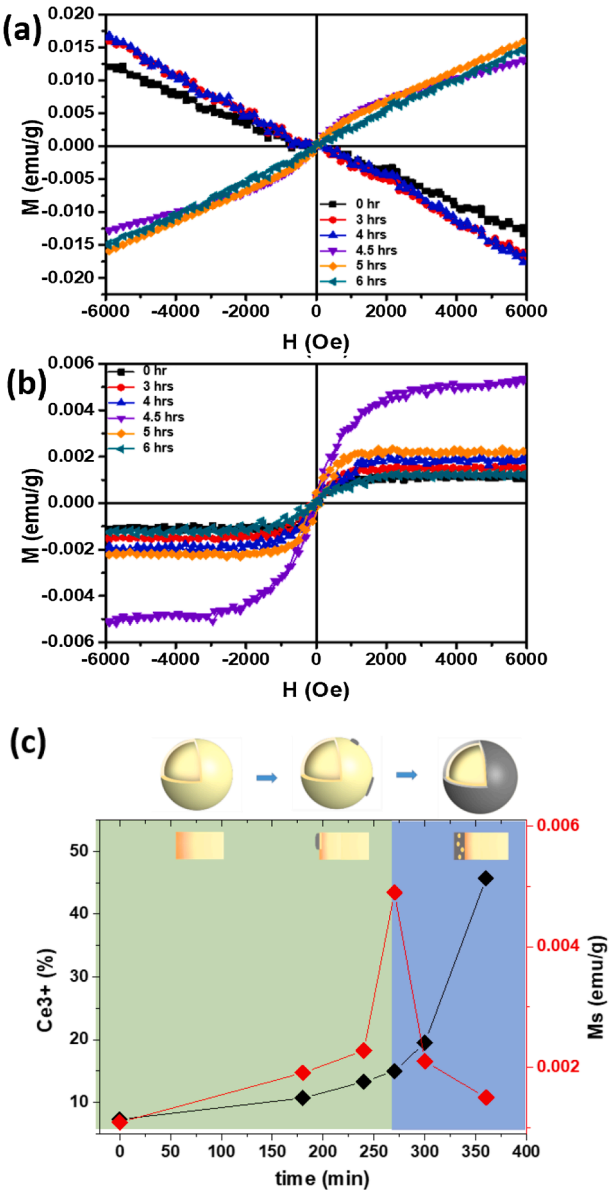


**Fig. 6.** (a) M−H curves before background subtraction of $CeO_2$ hollow spheres after reacting with citric acid for different times. (b) M−H curves after the background subtraction. (c) The variation of saturation magnetization, Ms, and $Ce^{3+}$ content with the reaction time of the treated samples. The evolution of microstructure with reacting time is illustrated in the insert figure.

As for the ferromagnetic properties, in ceria, it has been pointed out that its magnetic behavior is closely related to the $Ce^{3+}$ concentration on the surface of the sample and the continuity of the defect layer [13,14,19]. In present study, the content of $Ce^{3+}$ on the sphere surface, the interior of the sphere and the surface organic layer varies with the reaction time. As the reaction time increases from 0 h to 4.5 h, the increase in Ms can be attributed to the optimization of the surface defect layer structure. In the sample with the optimum $Ce^{3+}$ content and continuous structure (4.5 h- sample), the Ms value reaches the maximum value. Another origin for the ferromagnetism enhancement could be the presence of carbon. In both the $Ce^{3+}$-rich layer and the interior region, carbon was detected. Carbon-doped $CeO_2$ has been found to have ferromagnetic properties. Kumar et al. doped $CeO_2$ thin films with different amounts of C by means of ion implantation and found that it can improve its ferromagnetism [42]. Wu et al.'s first-principles calculation result believes that in C-doped $CeO_2$, C can provide magnetic moment and may make the material semi-metallic [43]. As the reaction time was further increased from 4.5 h to 6 h, the magnetic contribution of the surface defect layer was reduced by the formation of a thick organic layer, which simultaneously reduced the number of defects in the ceria spheres.

### 3.3. Optical properties

Fig. 7 shows PL spectra of the bare $CeO_2$ hollow spheres (0-hour sample) and the 6-hour sample measured at an excitation wavelength of 200 nm. The Fig. 7 (a) is the result obtained for dry powder and revealed several separated emission lines, notably in the 400 to 500 nm range, that are attributed to different defect levels in ceria [44,45,46]. Among them, the prominent blue emission at 470 nm is ascribed to surface defects [45,46]. Other lines have been reported from F-centers, oxygen vacancy, dislocations, allowed transition from $4f^7 \rightarrow 4f^6\ 5d^1$ states, etc [45]. At first, the presence of intense peak at 470 nm for both the 0-hour and 6-hour samples agrees with previous microstructural observations of ceria nanoparticles with defects highly concentrated at surface. The relative decrease of the 470 nm peak after 6 h confirms that surface defects are then reduced by the presence of the surrounding layer. Secondly, it is clearly seen that the emission in the 500–700 nm regions, where defect lines have weak influence, is more pronounced in the 6-

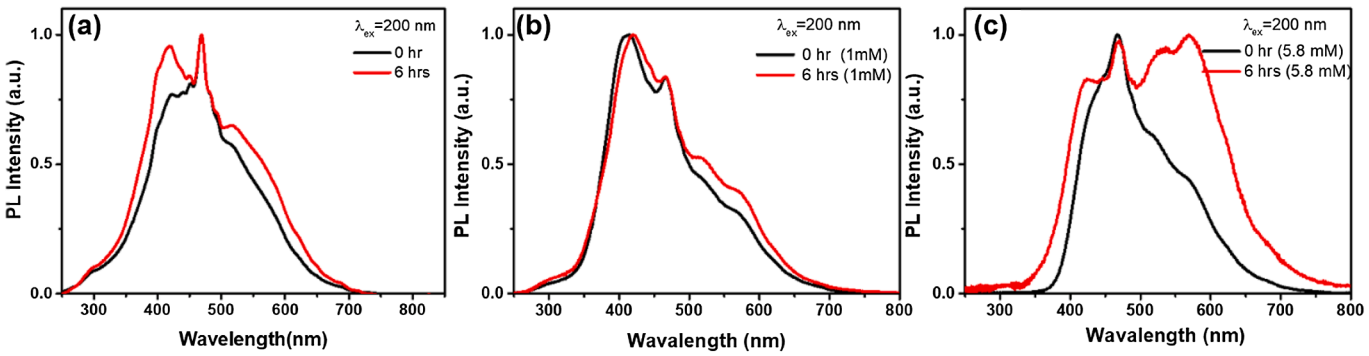


**Fig. 7.** PL spectra of the bare $CeO_2$ hollow spheres (0-hour sample) and the 6-hour sample measured at an excitation wavelength of 200 nm. The sample were measured in different condition, (a) dry powder state, (b) 1 mM solution, and (c) 5.8 mM solution.

hour sample.

Fig. 7 (b) (c) are the results obtained from aqueous samples. When the 0-hour sample is dispersed in water, the spectrum share similar shape to that of the dry state, but with a decreased visibility of the defect-associated lines. However, when the 6-hour sample is dispersed in water, the emission between 500 and 700 nm is significantly enhanced. This phenomenon is particularly evident when the solution concentration is high. Fig. S5 reports the emission spectra obtained with gradually increasing the excitation wavelength from 440 nm to 500 nm in 1 mM 0-hour and 6-hour solutions. A significant emission in the 500 to 600 nm is detected in the 6-hour sample solution while it is weak in the 0-hour sample solution. The observed red-shift phenomenon of the emission spectrum confirmed the fluorescence characteristics and is rather comparable with reported photoluminescence emission spectra of carbon dots [47].

Confocal fluorescence images of 0-hour and 6-hour sample are recorded under the excitations of 488 nm and 561 nm. As presented in Fig. 8 (a–b), only weak green fluorescence is detected in 0-hour sample. In 6-hour one, more intense green and red fluorescence is observed when excited at 488 nm and 561 nm respectively (Fig. 8 (d-e)). With merging the fluorescence images with bright field image, it shows that the green fluorescence is correlated to the ceria while the red fluorescence is majorly contributed by the surface Ce- organic layer (Fig. 8 (c) and (f)). Above fluorescence analysis pointed out that when the excitation energy is changed from high to low, the changes in PL properties observed in the 6-hour sample can be attributed to the defect lines associated with the ceria surface and the organic layer on the surface, respectively. As for the observed enhancement of the luminescence effect, it can be attributed to the interaction between the surface organic layer and the hollow spheres. Compared to carbon quantum dots alone, the organic layer in the 6-hour sample is continuous, with $Ce^{3+}$ clusters in it, and in contact with the inorganic ceria surface. This surface passivation has been shown to benefit the fluorescent properties of the inner material. Sun et al. doped the surface of core carbon nanoparticles with inorganic salts (ZnO, ZnS or $TiO_2$) and combined organic functionalization, to make carbon dots exhibit brighter fluorescence emission than undoped carbon

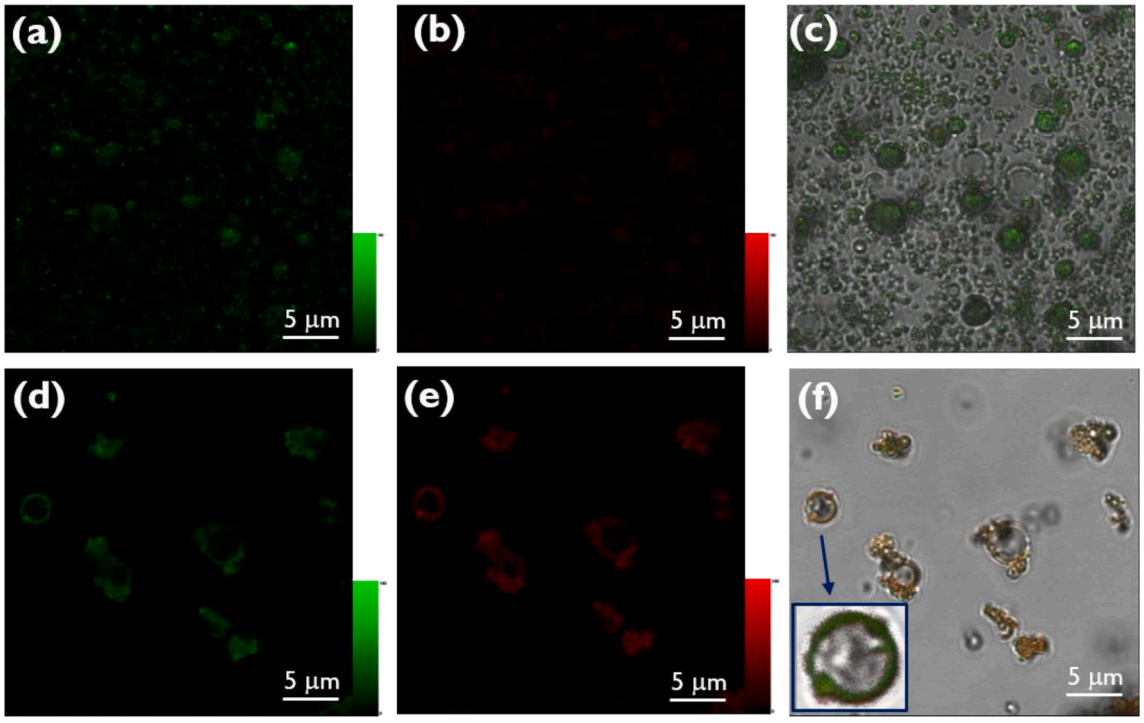


**Fig. 8.** Laser scanning confocal microscopy images of 0-hour and 6-hour samples. (a) Picture of 0-hour sample under excitation at 488 nm. (b) Picture of 0-hour sample under excitation at 561 nm. (c) Overlapping of confocal fluorescence images with bright field image of 0-hour sample. (d) Picture of 6-hour sample under excitation at 488 nm. (e) Picture of 6-hour sample under excitation at 561 nm. (f) Overlapping of confocal fluorescence images with bright field image of 6-hour sample.

dots [48,49]. Owing to the tunable magnetism and intense and multi-colored luminescence, these organic-ceria hybrid hollow spheres are promising materials in optoelectronic devices, imaging, and sensing.

## 4. Conclusion

In summary, we have developed an efficient approach for synthesizing a new organic – ceria core shell hollow spheres with dual-functions. The hybrid spheres are ferromagnetic at room temperature. The magnetic strength can be controlled by reaction time. The maximum Ms value is comparable to that obtained by reacting with nitric acid as well as annealing process. The magnetic variation trend of the samples can be explained by the synergistic effect of the ceria surface and interfacial reactions. Optical measurements demonstrated that the organic- ceria core shell hollow spheres exhibit red and blue emissions, which can be attributed to the $Ce^{3+}$-rich clusters doped organic layer and the $Ce^{3+}$-rich layer in the ceria sphere, respectively. In ceria, the study correlating its magnetism and optical properties is still rare. Our results can be used as a reference for future structural design.

*CRediT authorship contribution statement*

**Chien:** Formal analysis, Validation. **Bo-You Wu:** Formal analysis, Validation. **Pei-Kai Hsu:** Formal analysis, Validation. **Yi-Che Chen:** Formal analysis, Validation. **Jenn-Ming Song:** Conceptualization, Investigation, Resources. **Alexandre Gloter:** Methodology, Resources, Formal analysis, Writing – review & editing. **Shih-Yun Chen:** Investigation, Conceptualization, Formal analysis, Writing – original draft, Writing – review & editing, Supervision, Project administration, Funding acquisition.

## Declaration of Competing Interest

The authors declare that they have no known competing financial interests or personal relationships that could have appeared to influence the work reported in this paper.

## Acknowledgement

The authors would like to thank the Ministry of Science and Technology of the Republic of China, Taiwan, for financially supporting this research under Contract No. MOST 110-2112-M-011-001 and 111-2927-I-011-503.

## Appendix A. Supplementary material

Supplementary data to this article can be found online at https://doi.org/10.1016/j.apsusc.2022.153685.

## References

[1] C. Sun, H. Li, L. Chen, Energy Environ. Sci. 5 (2012) 8475.
[2] T. Montini, M. Melchionna, M. Monai, P. Fornasiero, Chem. Rev. 116 (2016) 5987–6041.
[3] L. Li, H.K. Yang, B.K. Moon, Z. Fu, C. Guo, J.H. Jeong, S.S. Yi, K. Jang, H.S. Lee, J. Phys. Chem. C. 113 (2009) 610.
[4] G. Vimal, K.P. Mani, P.R. Biju, C. Joseph, N.V. Unnikrishnan, M.A. Ittyachen, Appl Nanosci. 5 (2015) 837.
[5] S. Aškrabić, Z.D. Dohčević-Mitrović, V.D. Araújo, G. Ionita, M.M. de Lima Jr, A. Cantarero, J. Phys. D: Appl. Phys. 46 (2013), 495306.
[6] V. Seminko, P. Maksimchuk, V. Klochkov, S. Yefimova, J. Lumin. 242 (2022), 118605.
[7] I.N. Bazhukova, S.Y. Sokovnin, V.G. Ilves, A.V. Myshkina, R.A. Vazirov, N. Pizurova, V.V. Kasyanova, Opt. Mater. 9 (2019) 136.
[8] K. Ackland, J.M.D. Coey, Physics Report. 746 (2018) 1.
[9] A.T. Apostolov, I.N. Apostolova, J.M. Wesselinowa, Physica E Low Dimens. Syst. Nanostruct. 99 (2018) 202.
[10] W. Lee, S.Y. Chen, Y.S. Chen, C.L. Dong, H.J. Lin, C.T. Chen, A. Gloter, J. Phys. Chem. C. 118 (2014) 26359.
[11] W. Lee, S.Y. Chen, E.N. Tseng, A. Gloter, C.W. Ku, X.Y. Li, J. Magn. Magn. Mater. 464 (2018) 11.
[12] S.Y. Chen, Y.H. Lu, T.W. Huang, D.C. Yan, C.L. Dong, J. Phys. Chem. C. 114 (2010) 19576.
[13] V.K. Paidi, D.L. Brewe, J.W. Freeland, C.A. Roberts, J. van Lierop, Phys. Rev. B. 99 (2019) 180403(R).
[14] M. Li, S. Ge, W. Qiao, L. Zhang, Y. Zuo, S. Yan, Appl. Phys. Lett. 94 (2009), 152511.
[15] S.Y. Chen, E. Tseng, Y.T. Lai, W. Lee, A. Gloter, Nanoscale. 9 (2017) 10764.
[16] F. Hellman, A. Hoffmann, Y. Tserkovnyak, G.S.D. Beach, E.E. Fullerton, C. Leighton, A.H. MacDonald, D.C. Ralph, D.A. Arena, H.A. Dürr, P. Fischer, J. Grollier, J.P. Heremans, T. Jungwirth, A.V. Kimel, B. Koopmans, I.N. Krivorotov, S.J. May, A.K. Petford-Long, J.M. Rondinelli, N. Samarth, I.K. Schuller, A.N. Slavin, M.D. Stiles, O. Tchernyshyov, A. Thiaville, B.L. Zink, Rev. Mod. Phys. 89 (2017), 025006.
[17] Y. Qiu, W. Chen, S. Yang, B. Zhang, X.X. Zhang, Y.C. Zhong, K.S. Wong, Cryst. Growth Des. 10 (1) (2010) 177.
[18] E.N. Tseng, Y.T. Hsiao, Y.C. Chen, S.Y. Chen, A. Gloter, J.M. Song, Nanoscale. 11 (2019) 3574.
[19] P.K. Hsu, Y.C. Chen, A. Gloter, H.C. Chen, E.N. Tseng, S.Y. Chen, J.M. Song, Mater. Sci. Eng. B. 274 (2021), 115481.
[20] Y. Xiong, J. Ye, X.Y. Gu, Q.W. Chen, J. Magn. Magn. Mater. 320 (2008) 107–112.
[21] J.Q. Zheng, Y.F. Zhang, C.G. Meng, X.F. Wang, C.F. Liu, M.K. Bo, X.Y. Pei, Y. Wei, T.M. Lv, G.Z. Cao, Electrochim. Acta 318 (2019) 635–643.
[22] S. Lee, J. Yoon, W.S. Yoon, Y. Son, J. Alloy. Compd. 837 (2020), 155467.
[23] M. N. Volochaev, A. B. Granovsky, O. V. Zhilova, Yu. E. Kalinin, V. V. Ryl'kov, M. P. Sumets, V. A. Makagonov, S. Yu Pankov, A. V. Sitnikov, E. Fadeev, E. Lahderanta, V. A. Foshin, Superlattices and Microstructures 140 (2020) 106449.
[24] H.S. Hsu, Y.Y. Chang, Y.Y. Chin, H.J. Lin, C.T. Chen, S.J. Sun, S.M. Zharkov, C. R. Lin, S.G. Ovchinnikov, Carbon 114 (2017) 642.
[25] S.J. Sun, H.S. Hsu, S. Ovchinnikov, G.L. Chen, J. Magn. Magn. Mater. 432 (2017) 102–105.
[26] S. Zhu, Q. Meng, L. Wang, J. Zhang, Y. Song, H. Jin, K. Zhang, H. Sun, H. Wang, B. Yang, Angew. Chem. 125 (2013) 4045.
[27] W. Liu, S. Xu, Z. Li, R. Liang, M. Wei, D.G. Evans, X. Duan, Chem. Mater. 28 (2016) 5426.
[28] X. Hao, Z. Jin, J. Xu, S. Min, G. Lu, Superlattices Microstruct. 94 (2016) 237.
[29] M. Yan, Y. Hua, F. Zhu, L. Sun, W. Gu, W. Shi, Appl. Catal. B: Environ. 206 (2017) 531.
[30] H. Li, Y. Deng, Y. Liu, X. Zeng, D. Wiley, J. Huang, Chem. Commun. 55 (2019) 4419.
[31] A. Sharm, N. Tejwan, S. Thakur, V. Sharma, T.A. Singh, J. Das 124 (2022), 111995.
[32] J.R. McBride, K.C. Hass, B.D. Poindexter, W.H. Weber, J. Appl. Phys. 76 (1994) 2435.
[33] C.H. Chuang, Y.F. Wang, Y.C. Shao, Y.C. Yeh, D.Y. Wang, C.W. Chen, J.W. Chiou, S. C. Ray, W.F. Pong, L. Zhang, J.F. Zhu, J.H. Guo, Sci. Rep. 4 (2014) 1.
[34] J. Schwan, S. Ulrich, V. Batori, H. Ehrhardt, J. Appl. Phys. 80 (1996) 440.
[35] S. Honda, R. Tamura, Y. Nosho, A. Tsukagoshi, M. Niibe, M. Terasawa, R. Hirase, H. Izumi, H. Yoshioka, K. Niwase, E. Taguchi, K.Y. Lee, M. Oura, Jpn. J. Appl. Phys. 53 (2014) 02BD06.
[36] A. Mewada, S. Pandey, M. Thakur, D. Jadhav, M. Sharon, J. Mater. Chem. B. 2 (2014) 698.
[37] H. Ding, S.B. Yu, J.S. Wei, H.M. Xiong, ACS Nano 10 (2016) 484.
[38] S. Kurita, A. Yoshimura, H. Kawamoto, T. Uchida, K. Kojima, M. Tachibana, J. Appl. Phys. 97 (2005), 104320.
[39] P. Nachimuthu, W.C. Shih, R.S. Liu, L.Y. Jang, J.M. Chen, J. Solid State Chem. 149 (2000) 408.
[40] J.F. Xie, H. Zhang, S. Li, R.X. Wang, X. Sun, M. Zhou, J.F. Zhou, X.W. Lou, Y. Xie, Adv. Mater. 25 (2013) 5807–5813.
[41] Y.A. Wu, G.X. Lu, Phys. Chem. Chem. Phys. 16 (2014) 4165–4175.
[42] P. Kumar, F. Chand, K. Asokan, Mater. Res. Express. 4 (2017), 036403.
[43] S. Dai, W. Zhou, Y. Liu, Y.L. Lu, L. Sun, P. Wu, J. Phys. Chem. Solids. 116 (2018) 187.
[44] S. Kumar, A.K. Ojha, D. Patrice, B.S. Yadav, A. Materny, Phys. Chem. Chem. Phys. 18 (2016) 11157.
[45] N.M. Devi, N.K. Singh, Nanotechnology. 31 (2020), 225203.
[46] G. Wang, Q. Mu, T. Chen, Y. Wang, J. Alloys Compd. 493 (2010) 202.
[47] X. Wang, K. Qu, B. Xu, J. Rena, X. Qu, J. Mater. Chem. 21 (2011) 2445.
[48] Y.-P. Sun, X. Wang, F. Lu, L. Cao, M.J. Meziani, P.G. Luo, L. Gu, L.M. Veca, J. Phys. Chem. C 112 (2008) 18295–18298.
[49] P. Anilkumar, X. Wang, L. Cao, S. Sahu, J.H. Liu, P. Wang, K. Korch, K.N. Tackett II, A. Parenzan, Y.-P. Sun, Nanoscale 3 (2011) 2023–2027.